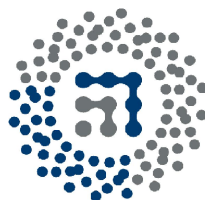Inter-University Master's in New Materials

MASTER'S PROJECT

Microwave synthesis and photophysical characterization of hybrid materials based on the encapsulation of dyes into unidirectional aluminophosphates

Presented by: Ainhoa Oliden Sánchez
Carried out at: Physical Chemistry Department

Under the direction of: Virginia Martínez-Mart

Leioa, $7^{th} of July$

Contents

Abstract

In this work, hemicyanine dyes LDS 722 and LDS 730 are encapsulated into the 1D nanochannels of MgAPO-11 and MgAPO-5 aluminophosphates via crystallisation inclusion method. The synthesis of the hybrid material has been optimized through a systematic variation of the crystallization conditions and gel composition in order to obtain the purest phase possible suitable for optical applications. The tight fitting between the molecular sizes of the guest dyes and the pore dimensions of the hosts has favoured a rigid planar conformation of the dyes. Consequently, the occlusion has led to a great enhancement of the fluorescence with respect to the dye in solution together with an alignment along the channels.

....

Resumen

En el presente trabajo, los colorantes LDS 722 y LDS 730 han sido encapsulados en 1D aluminofosfatos con canales unidireccionales de distinto tamano, MgAPO-11 y MgAPO-5, mediante el método de inclusión de cristalización. La síntesis del material híbrido se ha optimizado mediante una variación sistemática de las condiciones de cristalización y composición del gel, con el objetivo de obtener la fase requerida más pura posible para aplicaciones ópticas. El ajuste apretado entre los tamanos moleculares de los colorantes y las dimensiones de los poros ha favorecido una conformación planar rígida de los colorantes. En consecuencia, ha conducido a un gran aumento de la fluorescencia con respecto al colorante en disolución junto con una alineación de los colorantes a lo largo de los canales.

Chapter 1

Introduction

Bones, which give us stability, are the hardest and most rigid structures in the human body. Without bones, the human body would essentially be nothing more than a shapeless blob of tissue. Have you ever thought what they are made of? In fact, they are made of a natural hybrid material that consists of an inorganic and organic building block. This combination is the responsible for such strength, rigidity, and hardness.

Hybrid materials represent one of the fascinating developments in materials chemistry, which has given rise to an exponential increase in publications in recent years. One of the reasons is the tremendous possibilities they can offer by a combination of different properties of organic and inorganic components in a unique system, where the final properties are not a mere sum of the individual contributions of both moieties; new or enhanced characteristics can appear by synergistic effects, which are interesting in multiple areas such as optics, electronics, mechanics, energy and so on [1].

The nature of the interactions between the organic and inorganic fragments determines what type of hybrid compounds it is. **Class I** hybrid materials are those that the moieties are connected through weak interactions, such as Van der Waals, hydrogen bonding or weak electrostatic interactions. **Class II** hybrid materials, however, exhibit strong chemical interactions between the components, such as coordinated or covalent bonding [1].

An important family of **Class I** materials is denoted as a host-guest system where usually the guest is an organic compound of interest embedded into an inorganic matrix. One of the most used hosts are the zeolites or zeolitic materials. Natural zeolites were

discovered in the 30s, and were found to be useful as adsorbents and catalysts [2]. Generally, zeolites are microporous aluminosilicates that consist of a three-dimensional network and are characterised by large void volumes. The zeolitic structure is a regular inorganic framework formed by corner-sharing TO_4 tetrahedron (T=Si, Al), where each oxygen is shared between two tetrahedrons giving a porous structure. The intrinsic pores are usually filled with cations and water molecules. Hence, cations are required to compensate the net negative charge, because Si(IV) is replaced by Al(III) imparting a net negative charge to the framework. Therefore, the structural formula of a zeolite is described as $M_{2/n}$: Al_2O_3 : y SiO_2 : w H_2O, where n is the valence of the cation, $y/2$ is the Si/Al ratio (equal to or larger to two) and w represents the water enclosed in the zeolitic cavities. In most zeolitic structures the primary structural units, AlO_4 or SiO_4 tetrahedrons, are assembled into secondary building units which may be simple polyhedrons, such as cubes (see **Figure 1.1**), hexagonal prisms or cubo-octahedrons, giving rise to the final framework structure [3].
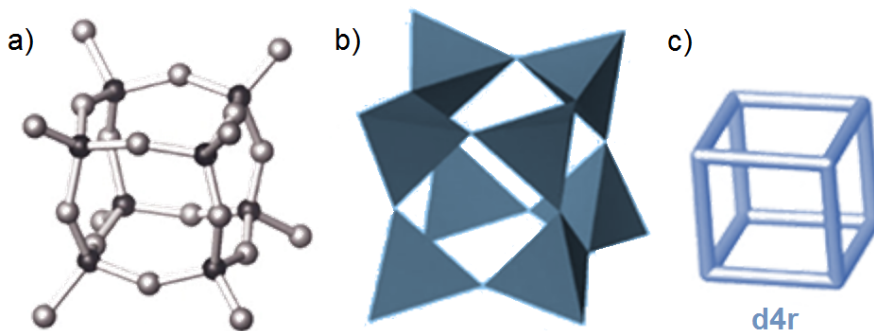

Figure 1.1: Common ways of representing the d4r (double four rings) composite building unit formed from eight tetrahedra in the shape of a cube. **a)** The standard view which represents T and O atoms as spheres. **b)** TO_4 tetrahedra with shared corners. **c)** A secondary cube building unit which has T-T linkages with the T-atom at the vertices and with oxygen atoms assumed to be positioned near the centre of each edge.

In this work, zeolitic inorganic structures called aluminophosphates (AlPO) are used as hosts in order to embed different organic dyes of interest with the objective of developing new hybrid solid materials with potential optical applications. These assemblages, analogous to zeolites, were discovered by Wilson et al. in 1983 [4]. The aforementioned frameworks are neutral, due to the alternation of AlO_4 and PO_4, containing channels and cavities with diameters ranging from 4 to 12 Å, depending on the structure [5].

However, occasionally a net charge into the aluminophosphate structure is required, like in this work in order to help the inclusion of cationic guest molecules. Thus, in this research, the divalent Mg (II) cation was used as a dopant to promote a negative charge into the aluminophosphate. This Mg^{+2} cation can adopt a tetrahedral coordination, and therefore Al^{+3} atoms are substituted in some sites of the framework without causing any perturbation in the final structure but generating Bronsted acid sites (**Figure 1.2**). The resulting material is called magnesium aluminophosphate or MgAPO.
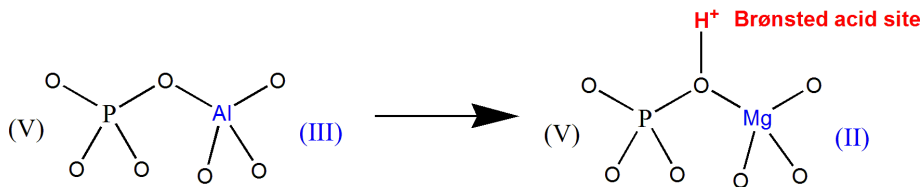

Figure 1.2: Schematic representation of the incorporation of Mg heteroatom into the AlPO structure to form MgAPO. This new framework is represented by a Bronsted acid site due to charge compensation.

Generally, by combining the photoactive dopant within the matrix, an improvement in chemical and physical properties, such as an increase in thermo- and photo- stability, are expected. Moreover, the final photophysical properties of a resultant hybrid material for a given dye, depends on factors such as the number of atoms forming the channel. In other words, the size and shape of the pore which will modulate the number of molecules within the channels and/or the degree or the type of aggregation exhibited by the encapsulated dye molecules. In this sense, systems with 1D-nanochannels with diameter sizes in the range of molecular dimensions are considered ideal hosts for a supramolecular organisation of photoactive guest molecules [6]. Therefore, highly fluorescent and orderly solid systems for the design of new devices with potential optical properties can be developed.

For that goal, different hemicyanine-type red-emitting dyes (LDS722 and LDS730, **Figure 1.3**) have been used in this work. Generally, the hemicyanine-type chromophores are aromatic compounds which contain a strong electron-donating group at one end of their molecular structure and a strong electron-withdrawing group in the opposite end, connected through methylene groups. In this case, the electron-donating group is aniline, and the electron-withdrawing group is pyridinium in LDS 722 and pyrrolium in LDS 730, respectively.

These dyes usually have high absorption capacity in the blue-green region of the visible spectrum. However, their fluorescence band appears very red-shifted with respect to the

main absorption band. This large Stokes shift is a consequence of their "push-pull" nature since the fluorescence emission arises from an intramolecular charge transfer state (ICT). These are advantageous features for minimising the inner filter, particularly interesting for laser applications and NLO applications such as Second Harmonic Generation (SHG) or two photon absorption (TPA).
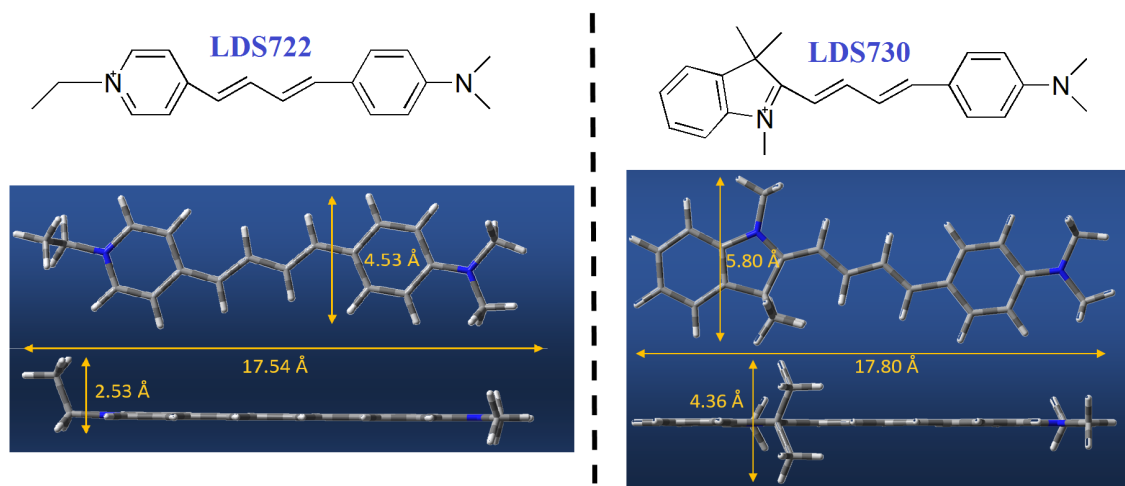

Figure 1.3: Molecular structures of red-emitting dyes (LDS 722 and LDS730) with their respective dimensions calculated by optimizing the ground geometry using B3LYP hybrid functional (DFT) via Gaussian 09.

However, these very flexible molecules usually present poor fluorescence quantum yields in solution due to rotational motions around the different bonds, giving rise to non-radiative deactivation such as cis-trans isomerization or the formation of non-fluorescent twisted intramolecular charge transfer states (TICT). In this sense, a tight confinement of these dyes in a 1D-nanoporous host will be interesting to limit its flexibility and induce an aligned arrangement of the dyes along the channels. It should be noted that the pore openings of the zeolitic hosts must tightly fit with the molecular dimension of the dyes (see **Figure 1.3**). Because of all the above mentioned, a couple of MgAPO structures, MgAPO-11 (AEL structure type, see **Figure 1.4a**) and MgAPO-5 (AFI structure type, see **Figure 1.4b**) were selected as host systems for LDS722 dye and LDS730, respectively.

Both host matrices show one-directional elliptical channel systems. In MgAPO-11, these channels are composed of rings of 10 tetrahedrons (10 MR), and they have a dimension of 4 x 6.6 Å. It is noteworthy in this structure that it possesses a special channel-topology, containing pockets along the channel direction (see **Figure 1.4a**).
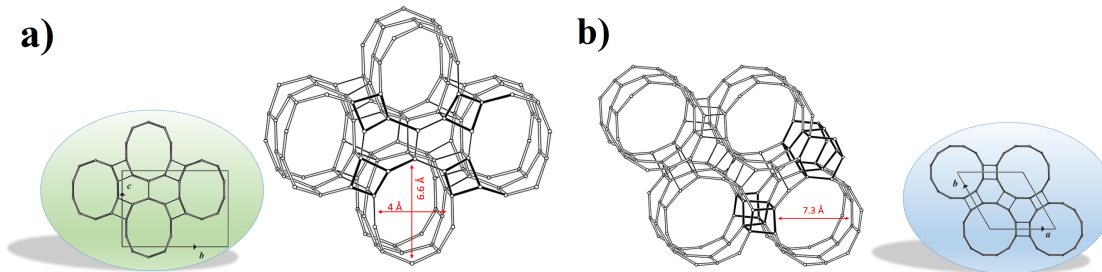
Figure 1.4: a) Structure of AEL, MgAPO-11. **b)** Structure of AFI, MgAPO-5.

On the other hand, MgAPO-5 is composed of alternating AlO_4 and PO_4 tetrahedron, forming a one-dimensional framework which contains electrically neutral cylindrical channels of uniform cross sections (7.3 Å) extended parallel to the long (c) axis of the crystals (see **Figure 1.4b**) [7].

However, the inclusion method of the dyes can drastically affect the optical properties of the material. In this work, the crystallisation inclusion method will be performed, which means that the dyes are incorporated "in situ" during the crystallisation of the material, adding them directly to the synthesis gel together with the specific agent that directs the structure (SDA: Structure Directing Agent). This methodology allows the inclusion of molecules whose size matches tightly with the opening of the pores of the zeolitic material, imposing a high-energy barrier for intracrystalline diffusion.

Nevertheless, it has to be taken into account that the organic dyes must be soluble in the synthesis gel (mainly aqueous) and not affect the final phase of the material. Previous syntheses performed in the group by conventional hydrothermal synthesis have given rise to very promising results [8]. However, the incorporation of the dye along the channel in some situations has been scarce and/or inhomogeneous and has generated other minority phases.

Another aim of this work is to optimise the synthesis by means of a microwave as an alternative technique with the objective of cutting times, generating fewer by-products and also obtaining more homogeneous incorporations of the dyes. The previous hydrothermal synthesis done for similar hybrid systems in conventional ovens are typically performed from aluminophosphate gels containing organic templates at 150-200°C with times ranging from several hours to several days. In this way, crystallisation times can be drastically reduced and in some cases, the zeolite crystal size can be substantially decreased to nm size.

In this context, the most important benefit of applying microwave irradiation (MW) is that the synthesis mixtures can be rapidly heated to the desired temperature. Moreover, the direct energy transfer to the synthesis gels by MW offers a homogeneous heating and thus avoids the unwanted temperature gradients often encountered during conventional electrical heating (see more advantages in **Figure 1.5**).
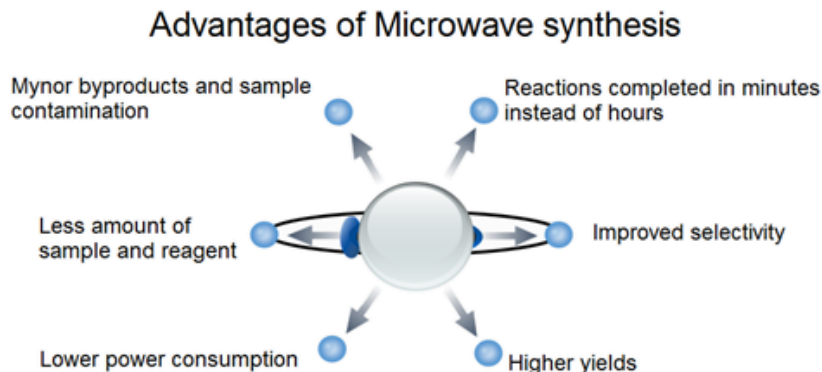
Advantages of Microwave synthesis

Mynor byproducts and sample contamination

Reactions completed in minutes instead of hours

Less amount of sample and reagent

Improved selectivity

Lower power consumption

Higher yields

Figure 1.5: Several benefits of applying microwave synthesis instead of conventional electrical heating.

Hence, the hydrothermal synthesis of aluminophosphate molecular sieves via MW was attempted to increase the efficiency of the synthesis to achieve fast crystallisation, high phase purity, and narrow particle size distribution [9]. First, the optimisation of the synthesis of the two MgAPO frameworks was performed in order to achieve, if possible, pure phases. In this sense, different reaction conditions (i.e. the heating ramp and the crystallisation temperature) and different gel compositions (i.e concentration of the organic template and/or magnesium) were tried.

Then, the organic dyes were encapsulated by crystallisation inclusion method with the aim of obtaining interesting systems for optical applications. The resultant hybrid materials were deeply characterised by several spectroscopic techniques.

Chapter 2

Experimental Section

In this chapter, the synthesis procedures of the two-different magnesium aluminophosphates with and without dye by microwave technique, followed by the instrumental techniques utilised for characterizing the final materials are described. X-Ray diffraction (XRD) was used for all samples to identify the final phases. Finally, several photophysical techniques (absorption and emission spectroscopies and fluorescence microscopy) employed for the characterization of the optical materials synthesized in this work are also described.

In general, the characterization is essential to assess the usefulness of the microwave assisted synthesis technique applied to obtain the desirable crystal phase with improved optical properties relevant for potential applications.

2.1   Synthesis of MgAPO materials

The synthesis of MgAPO hybrid materials was carried out via hydrothermal synthesis, based on sol-gel chemistry. The microporous magnesium aluminophosphates were prepared using phosphoric acid (Aldrich, 85 wt%), magnesium acetate tetrahydrate (99 wt%, Aldrich), aluminium hydroxide (Aldrich), triethylamine (TEA, Aldrich), ethylbutilamine (EBA, Aldrich), LDS 722 (Exciton) and LDS 730 (Exciton) from gels with molar compositions of xMgO:1 P_2O_5: (1-$\frac{x}{2}$) Al_2O_3: ySDA: z Dye : 300 H_2O, where the SDA was EBA (for AEL phase) or TEA (for AFI phase) being x = 0.1 or 0.2 , y = 0.75 or 1 and z varying from 0.008 to 0.024 (see **Table 3.1** in result section). Note that highly diluted gels are

prepared, to ensure the solubility of the dyes in water.

The synthesis was performed following these steps: i) phosphoric acid was mixed with water in a polypropylene vessel and it was kept under vigorous stirring for 2 minutes; ii) next, the magnesium source, in our case, magnesium acetate tetrahydrate, was added to the reactive mixture; iii) then, aluminium hydroxide, as the aluminium source, was gently added; iv) the resultant mixture was left under stirring for another 5-10 minutes and the structure directing agent (SDA) was added to the reaction gel without the dye.

Since the aim of this work is to obtain dye-doped magnesium aluminophosphates, the organic dye was added to the synthesis gel at the last point. Thus, the dye was incorporated by the so-called crystallization inclusion method. Afterwards, the mixture in the vessel was covered with a film and it was kept under stirring for one hour before measuring the pH of the gel. The pH values of the different gels were between 3 and 5. At that point, the mixture was transferred to a Teflon liner (100 ml), leaving an empty space of around two-thirds of the total volume of the container to ensure an optimal pressure, and then was closed into a teflon autoclave (**Figure 2.1**). The aqueous mixture was then heated statically in the teflon autoclave in an ETHOS Advanced Microwave Digestion system (Milestone) at temperatures between 145 and 195° C and at 500W, under autogenous pressure, and for reaction times no longer than 2h. To ensure that there were no losses, the autoclave was weighted before and after the reaction process in the microwave. The resulting material was recovered by filtration (Scharlab S.L, 2-3 μm retention), exhaustively washed with distilled water and ethanol, and dried overnight.
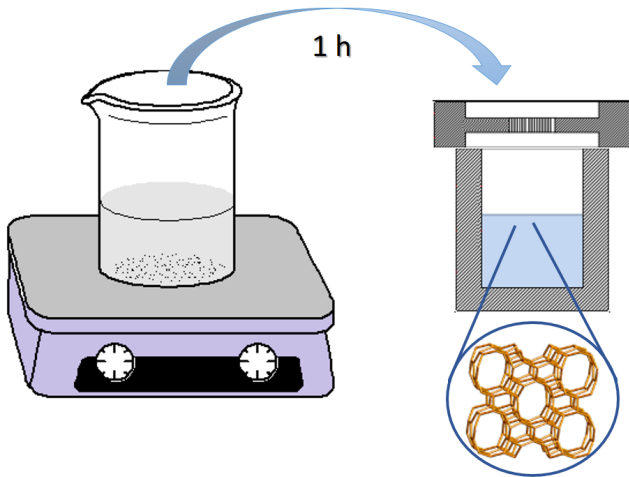

Figure 2.1: Synthesis procedure for the magnesium aluminophosphates.

In a typical preparation of MgAPO-11, 1.60 g phosphoric acid are mixed with 37.13 g water and 0.30 g magnesium acetate tetrahydrate. Then 0.96 g aluminium hydroxide and 0.70 g EBA added over this mixture, together with the required amount of dye in each case, to yield the previously described gel composition. For the synthesis of MgAPO-5 the same procedure was carried out, but changing the amount of template to 0.53 g of TEA.

2.2   Structural characterization

- **X-ray powder diffraction (XRD)**

  These measurements were carried out at the University of the Basque Country, SGIker. X-ray powder diffraction patterns were collected by using a Philips X'pert PRO automatic diffractometer operating at 40 kV and 40 mA, secondary monochromator with Cu-K radiation (λ= 1.5418 Å) and a PIXcel solid state detector (active length in 2θ 3.347º). Data were collected from 5 to 80, 2θ (step size 0.026 and time per step 60 s) at RT. A fixed divergence and anti-scattering slit giving a constant volume of sample illumination were used. A model adjustment without a structural pattern (Pattern matching) was made for each sample in order to make a semi-quantitative analysis.

- **Scanning Electron Microscopy (SEM)**

  The size and morphology of the MgAPO materials were characterized by Scanning Electron Microscopy (SEM) in a JEOL JSM-6400 (tungsten filament) and in a JEOL JSM-7000F (Field Emission Gun) operating at 20 kV and 10^{-11} A at the University of the Basque Country (SGIker).

2.3   Dye loaded quantification

The final dye uptake incorporated in the MgAPO power was quantified spectrometrically, after dissolving a certain amount of the sample powder in hydrochloric acid (5 M). The absorption spectra of the samples were compared with the spectra of the standard solutions prepared from known concentrations of the dyes in analogous conditions. The absorption

spectra were recorded with a UV-Vis spectrophotometer (Varian, model Cary 4E), described later in detail **(Section 2.4)**. Dye content values are given throughout this work as mmol dye per 100 g sample powder and in percentage with respect to the initial amount added in the synthesis gel.

2.4 Photophysical characterization

In the current section, the experimental techniques employed for the photophysical characterization of all the systems studied in the present work are described. The techniques used range from spectrometry (UV-Vis) and spectrofluorimetry (steady-state and time-correlated) for both solid and liquid samples (measured in cuvettes of 1 cm).

Absorption spectra of liquid samples (samples and standards for the dye-loading quantification and the dyes used were recorded with a double beam UV-Vis spectrophotometer (Varian, model Cary 4E). The spectrometer has two emission lamps: a halogen lamp (for the visible region) and a deuterium lamp (for UV region), which are exchanged at 350 nm. The Cary 4E has a double monochromator with 1200 lines/mm with ± 0.1 nm resolution and a Hamamatsu R928 photomultiplier as a detector (**Figure 2.2a**). Absorption spectra were recorded in transmittance from 200 to 800 nm, at 120 nm/min and with a slit width of 1 nm. Signal was corrected placing the solvent which corresponds to the reference beam. In the case of dye-loading quantification in MgAPO samples, MgAPO powder without dye, dissolved in the same conditions as the sample under study, was used as a reference.
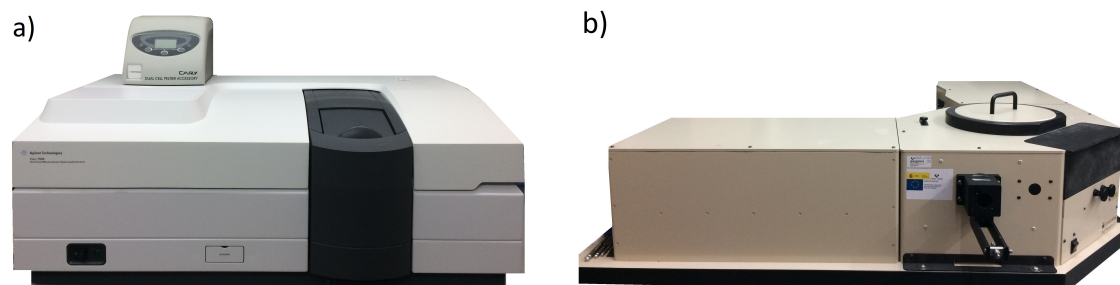

Figure 2.2: a) Double beam UV-Vis spectrophotometer (Cary 4E). **b)** Edinburgh Instruments Spectrofluorimeter, FLSP920 model.

The absorption spectra of the dye/MgAPO powder samples were recorded by means of an integrating sphere (Internal DRA 900), which detects the reflected light. The respective spectra of MgAPO crystals synthesized in identical conditions but without dye were recorded and subtracted from the sample signal to eliminate the scattering contribution of the particles to the absorption spectra.

Steady-state luminescence spectra were measured in an Edinburgh Instruments Spectrofluorimeter (FLSP920 model, **Figure 2.2**b), with 450W continuous xenon arc lamp as the excitation source (Xe900 model, poner detector IR acoplado). Fluorescence spectra were corrected from the wavelength dependence of the detector sensitivity.

Absolute fluorescence quantum yields of powder samples were measured in the same spectrofluorimeter by means of an integrating sphere and with a Spectralon white scatter as a reference.

Fluorescence decay curves were carried out in the above-cited Edinburgh Instruments Spectroflurimeter, by means of the Time Correlated Single Photon Counting technique [10][11]. Fluorescence decay curves were monitored at the emission maximum (after collecting 10000 counts at the channel with the maximum intensity) exciting the samples by means of a Fianium supercontinuum wavelength-tunable laser with 150 ps FWHM pulses. The erratic scattering signal of the laser was avoided in the detection channel by filtering the excitation light with the corresponding cut off filter (Lambda Research Optics, Inc.) placed between sample and detector. A repetition rate of 10 MHz, in time-windows ranging between 50-100 ns and a power of around 0.5 mW was used.

Fluorescence lifetimes (τ) were obtained from the slope after the deconvolution of the instrumental response signal from the recorded decay curves by means of an iterative method by the FAST software (Fluorescence Analysis Software Technology). The goodness of the deconvolution process was controlled by the chi-square (χ^2) statistical parameter and the residuals analysis.

Usually, in solid samples, a multiexponential behaviour is observed, and it is typically ascribed to the high heterogeneity degree of the environment in which molecules are embedded, in comparison with the solution [12][13]. Thus, the decay curves are adjusted to a sum of exponential decays by means of equation **1**.

$$I_{fl}(t) = \Sigma_i A_i e^{-t/\tau_i} \qquad \textbf{(1)}$$

where A_i are the pre-exponential factors related to the statistical weights of each exponential, and τ_i are the fluorescence lifetimes of each exponential decay. Due to the difficulty to give a physical interpretation of the multi-exponential curves, an average lifetime τ is considering according to the equation **2**:

$$< \tau >_{ia} = \Sigma A_i \tau_i^2 / \Sigma A_i \tau_i \qquad \textbf{(2)}$$

which represents the average lifetime that the molecules spend in their excited state.

Fluorescence images were recorded with an optical upright microscope with epi configuration (Olympus BX51), where the emission is collected in the same direction of excitation, equipped with a color CCD camera (DP72). As excitation source a 120 W short arc lamp that provides white light was used (X-Cite$^{\textcircled{R}}$ Series 120Q, EXFO). Excitation radiation and emission range were selected by Chroma band pass and cut-off filters, respectively. For polarized emission experiments, a polarizer (U-AN-360–3) was incorporated before the registration of the image in the CCD camera.

2.5   Computational methods

The direction of the transition dipole moment and the electronic densities of LDS722 and LDS730 were calculated performing quantum mechanics calculations by Gaussian 09 [14]. The ground geometry was fully optimized with the B3LYP (Becke, three-parameter, Lee-Yang-Parr) hybrid functional (DFT).

Chapter 3

Results and discussion

3.1 Optimization of MgAPO-11 synthesis

The different MgAPO-11 materials were prepared under microwave heating according to a previous recipe adapted from Virginia et al.[6] and using the following gel molar composition:0.2 Mg0:1 P_2O_5:0.9 Al_2O_3:1 EBA:300 H_2O.

Table 3.1: Experimental conditions (crystallization times and temperatures) used for the preparation of microwave MgAPO-11 samples, initial and final pH values and respective phases obtained in the synthesis.

Sample	T (°C)	Time (min)	Phases (%)		pH	
			AEL	Impurities	Initial	Final
1	145	20		Amorphous	4.4	3.8
2	145	40	37	63 AFI	4.4	4.5
3	145	60	25	75 AFI	4.4	4.7
4	170	10	31	70 AFI	4.3	4.8
5	170	20	55	45 AFI	4.3	4.7
6	170	40	45	55 AFI	4.3	4.8
7	170	60	44	66 AFI	4.2	4.8
8	195	20	42	58 AFI	4.2	5.2
9	195	40	43	57 AFI	4.2	5.2
10	195	60	56	44 AFI	4.2	4.9
11	195	120	61	24 AFI, 10 Others	4.3	5.1

Highly diluted gels were employed to favour the synthesis of large and single crystals, and at posteriori to enable the dissolution of the dye in the aqueous synthesis gels since the solubility of the chromophores in water is relatively low.

In a first step, for MgAPO-11 samples, an optimization of the MW parameters was performed in order to find the optimal conditions for achieving AEL phase in the synthesis. Therefore, the respective gels were heated at different temperatures, during different periods of time using a ramp time (i.e. the time to reach the desired crystallization temperature) of 2 min. **Table 3.1** summarizes the different synthesis conditions used along this study.

Figure 3.1 shows the XRD patterns obtained for the different MW synthesized samples. In fact, AEL and AFI type structures are recorded in all of them. In the diffractograms registered for the samples, the most characteristic peak of MgAPO-11 is detected at $2\theta = 10.9$ ^{o}, in addition to smaller features around 9° and 21° 2θ. However, the presence of MgAPO-5 impurity is evident, recording its most intense peak at $2\theta = 7.4$ ^{o}.
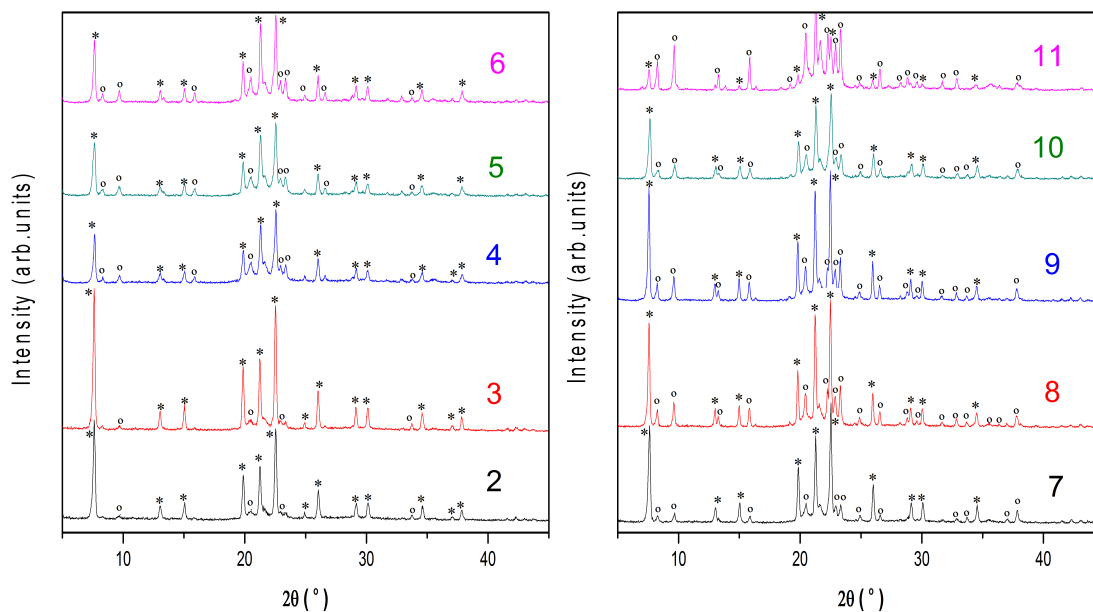

Figure 3.1: XRD patterns of samples 1-11; marks ^{o} denote peaks from AEL phase while * denote peaks from AFI phase. Sample 1 pattern is not included as no peaks were observed (amorphous phase).

Firstly, the effect of synthesis temperature on the formation of MgAPO-11 crystals was studied (**Table 3.1**). At a relatively low temperature of 145 ºC an amorphous solid

was obtained. Generally, when the temperature was reduced, the speed of crystal growth is significantly decreased and hence the formation of X-ray detectable AEL crystalline solid could only be achieved for longer times (in particular, in samples 2 and 3, **Table 3.1**). According to these patterns, one can see that samples obtained at low temperatures (145ºC, samples 2 and 3) present a small amount of AEL phase, achieving mainly AFI phase. However, increasing the microwave temperature leads to the formation of AEL phase remarkably, doubling the amount of final AEL phase from 25% to 56% (sample 3 and 10, **Table 3.1**) at 60 minutes (**Figure 3.2**a).
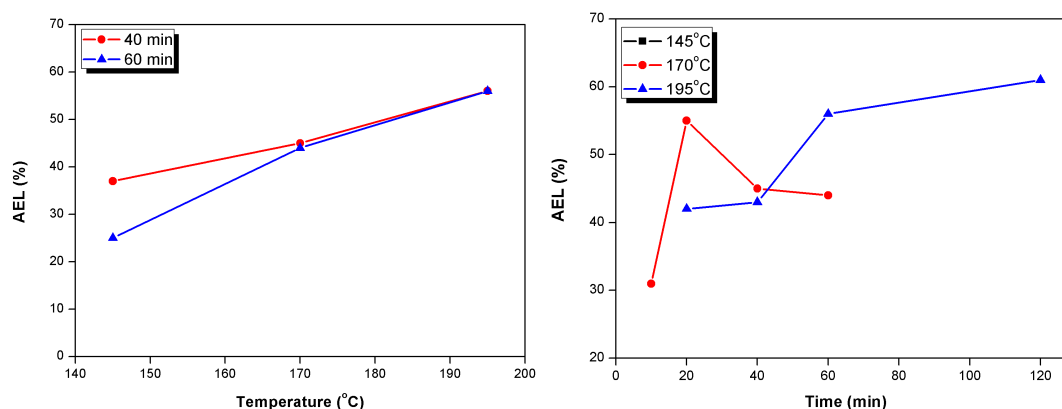

Figure 3.2: Purity plots of AEL phases (in percentages) achieved at various reaction **a)** temperatures and **b)** times.

A relationship between the crystallization time and the crystal purity was found too, (**Figure 3.2**b). By increasing the reaction time, a higher content in MgAPO-11 is obtained, with the incomprehensible exception in sample 5. This statement is not fulfilled in the samples 2 and 3 either, due to the low crystallization temperature applied in the synthesis. On this basis, the best sample with the higher content was achieved at 120 min with an AEL content of 61% (sample 11 in **Table 3.1**), with AFI as secondary phase. Hence, at first glance it seems that the time is responsible for stabilizing MgAPO-11 and destabilizing AFI; nonetheless, besides AEL it also stabilizes other phases which have been obtained as impurities at longer times.

The kinetics of crystal growth is temperature dependent, and the temperature is a more effective parameter for the adjustment of the crystallite size compared with the heating time. A high temperature accelerates the speed of the gel dissolution and increases the rate of nuclei growth. Nucleation is thought to be favoured at lower temperatures. As a result, MgAPO-11 crystals with larger sizes were achieved at higher temperatures (195

°C).

On the other hand, **Figure 3.3** shows the SEM images of the samples synthesized at 195°C but at different crystallization times. Interestingly, a longer heating time during the syntheses did have a high effect on the crystallinity of the crystals formed (**Figure 3.3**). Moreover, for almost all samples non-crystalline phases could be observed at a time of 60 min.Two morphologies are presented, which confirms the previous results, i.e. the presence of AEL and AFI structures, characterized as a plate shape crystal morphology and hexagonal rod structure, respectively. As a consequence, higher times should be required in order to achieve purer and more crystalline samples.
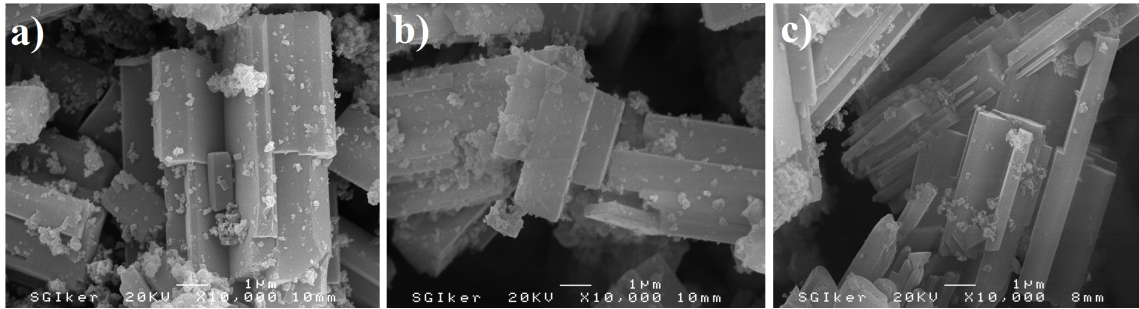

Figure 3.3: SEM micrographs of samples synthesized at different heating times: **a)** Sample 8; **b)** Sample 9; **c)** Sample 10.

Another attempt to favour the formation of MgAPO-11 and to reach higher purities, was focus on the systematic variation of the composition of the synthesis gel (amount of Mg and structure directing agent, SDA, ethyl butylamine (EBA) by following the general gel molar composition: $xMgO$: 1 P_2O_5: $(1-\frac{x}{2})$ Al_2O_3: $ySDA$: 300 H_2O.

For higher Mg amount in the gel (x=0.2) the presence of AFI is noticeable (**Table 3.2**, **Figure 3.4**). However, when x is reduced to 0.1 no MgAPO-5 is observed, even though extra impurities appear such as dense phases and another type of phosphates are found.

While decreasing the template from 1.0 to 0.75 and maintaining the magnesium content 0.2, a substantial drop was noticed respect to the MgAPO-11 content. However, following the same procedure for Mg 0.1, rather the contrary was observed. Note here that the heating time effect also favoured the growth of AEL crystals, obtaining a major content of AEL for those made at 120 min compared with the ones made at 60 min (**Table 3.2**, **Figure 3.4**).

Overall, the best experimental condition to obtain the highest amount of AEL phase

Table 3.2: Different gel composition synthesis conditions with their respective phases achieved together with the initial and final pH-s.

Sample	x	y	Time (min)	Phases (%)		pH	
				AEL	Impurities	Initial	Final
10	0.2	1	60	56	44 AFI	4.2	4.9
11	0.2	1	120	61	24 AFI, 10 Others	4.3	5.1
12	0.2	0.75	60	15	19 SiO_2, 66 Others	3.4	4.3
13	0.2	0.75	120	38	9 AFI, 53 Others	3.5	4.4
14	0.1	1	60	28	23 SiO_2, 49 Others	3.3	4.8
15	0.1	1	120	39	61 Other	3.4	4.9
16	0.1	0.75	60	34	9 SiO_2, 57 Others	3.1	4.6
17	0.1	0.75	120	46	54 Others	3.2	4.8

was achieved in sample 11 (**Table 3.2**). Nevertheless, Rebeca et al. [8] founded that when LDS 722 dye is added to the synthesis gel under conventional heating with a Mg content of x= 0.2, MgAPO-5 phase is favoured with respect to MgAPO-11 , even at a high temperatures (195ºC). Thus, particularly for this dye, an amount of Mg of x = 0.1 is recommended; therefore, for these stated reasons, the synthesis conditions of sample 11 and 13 were dismissed and the conditions employed in sample 15 and 17 were selected for the encapsulation of the LDS 722 dye. Moreover, in sample 15 only one impurity was found, what makes it an extraordinary candidate for the occlusion.
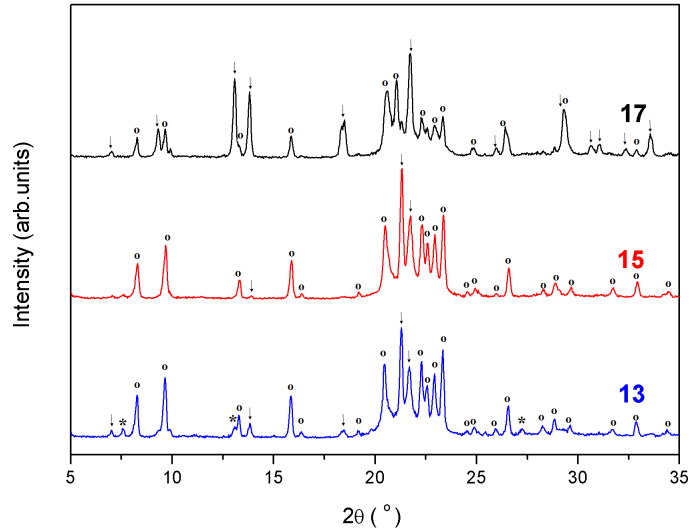

Figure 3.4: XRD patterns of samples 13,15 and 17; marks ^{o} denote peaks from AEL phase while * denote peaks from AFI phase and arrows denote peaks from impurity phases.

3.2 Dye occlusion into MgAPO-11 host systems

As cited above, with the aim of boosting the emission capacity of LDS 722 dye and obtaining a preferential orientation along the channels, LDS 722 will be tightly encapsulated into 1D-nanochannels of MgAPO-11. Due to the perfect match between the dye molecular dimensions and the pore size, the crystallization inclusion method should be applied. In this context, the gel compositions from 15 and 17 samples are used, and a dye amount in a molar ratio of z= 0.008 and 0.024 is directly added to the gel. The indicated experiments are shown in **Table 3.3**.

Table 3.3: Gel composition: xMgO: 1 P_2O_5: (1- x) Al_2O_3: ySDA: 300 H_2O and z dye content added to the samples. The amount of dye loaded in each sample is expressed as mmol of dye per 100 grams of solid product and as a percentage of the dye loaded with respect to the initial amount of the gel.

Sample	x	y	z	Phases (%)		mmol/100g	Dye uptake (%)
				AEL	Impurities		
15A	0.1	1	0.008	68	32 Others	2.42	55
15B	0.1	1	0.024	32	33 AFI, 35 Others	8.16	71
17A	0.1	0.75	0.008	27	10 AFI, 63 Others	1.90	47
17B	0.1	0.75	0.024	56	44 Others	8.52	72

First of all, the syntheses done with different amounts of the structure directing agent (15A vs 17B, or 15B vs 17B) do not play any particular role towards the dye uptake as the final amount reached were very similar (55% and 47% for sample 15A and 17A and values 71 and 72% for 15B and 17B).

However, the amount of dye and template added to the synthesis gel made an important impact in the purity of the AEL final reached. In this sense, the experiment derived from the synthesis condition 15A yielded MgAPO-11 as the major phase, though with a minor presence of other structures as impurity phases (**Figure 3.5a**). Those crystals were pink in colour, while the other samples showed different brown hues and dark violet colours (**Figure 3.5b**).

The amount of dye taken up by the solid 15A was relatively high, 2.42 mmol per 100 g material, which represents the 55% of the total dye added to the gel. More importantly, this sample shows a red-pink emission colour (**Figure 3.5b**), with important fluorescence efficiency interesting for optical applications. In comparison, its analogous sample with a higher amount of dye in the initial gel (z =0.024), sample 15B, has rendered a much lower

AEL phase and much higher content of dye occluded ($\succ$8 mmol per 100 g material, **Table 3.3**), though no signs of fluorescence were noticed under UV light. Same results in term of fluorescence was obtained for the sample 17B, with similar dye content but higher amount of AEL phase (**Table 3.3**). These results are attributed to the reabsorption/reemission effects, important at higher dye concentration, giving rise to inner filter effects which involes an abruptly decrease in the fluorescence yields of the samples.
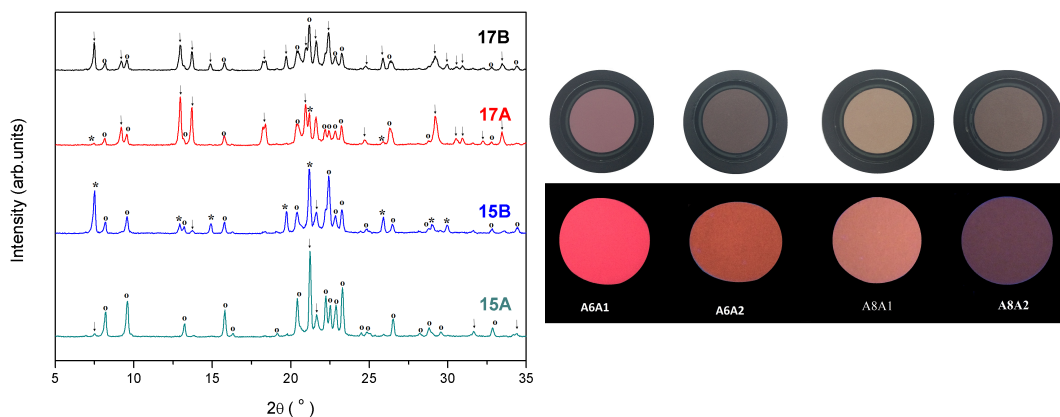
Figure 3.5: a) XRD patterns of samples 15A,15B, 17A and 17B; marks ^{o} denote peaks from AEL phase while the arrows denote peaks from impurity phases. **b)**LDS 722/AEL samples under ambient and UV light.

SEM photographs of MgAPO-11 crystals obtained for samples 15 and 15B (data not shown) show the same AEL morphologies (plate-like morphology as stated before), adding any dye or not. On this account, the photophysical properties of 15A sample were thoroughly analysed to remark the optical enhancement fulfilled during this project.

As stated before in the introduction, styril dyes and particularly LDS 722, have high absorption capacity in the blue region of the visible spectrum and typically show large Stokes shift, which is consequence of an intramolecular charge transfer favoured upon excitation (ICT, see **Figure 3.6a**). Since the rotamerism process takes place via different pathways around different single and double bonds, the molecule undergoes internal rotations that leads to several twisted intramolecular charge transfer. This phenomenon implies a poor fluorescence quantum yields (**Table 3.4**) and very short lifetimes (**Figure 3.6b**) in solution due to the rise in non-radiative deactivation processes.

This behaviour is related to the nature and structure of the hemicyane dyes (**Figure 3.7**), which have an electron donor group on one side (amino group), while on the other it has an electron-withdrawing alkyl pyridinium group. These charge transfer process is
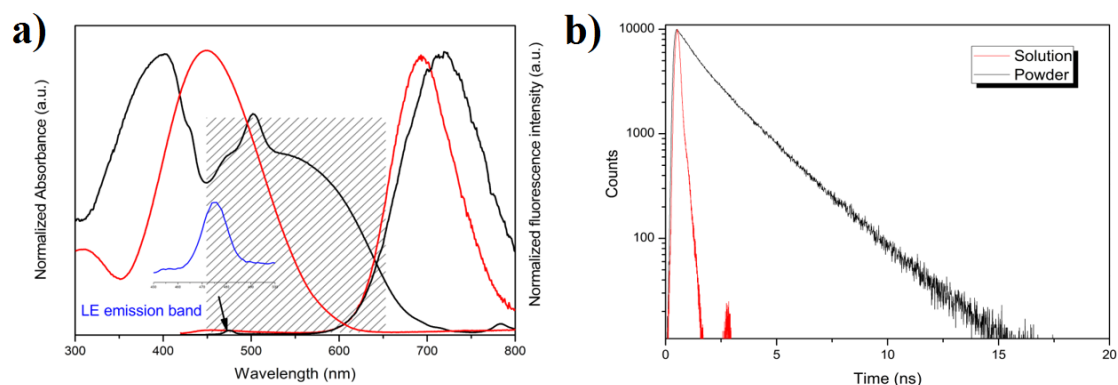
Figure 3.6: a) Height normalized absorption and emission spectra recorded for the dye LDS 722 in aqueous neutral solution (red) together with LDS 722/AEL powder (Sample 15A, black) **b)** Fluorescence decay curves for the dye LDS 722 in powder (black) and solution (red).

verified by the electronic densities of the molecule in fundamental (HOMO) and excited states (LUMO) as demonstrated by computational calculations depicted in **Figure 3.7**. In these calculations, it can be seen that a higher electronic density is located in the amino group in the HOMO state, while in the LUMO it is placed in the alkyl pyridinium, indicating that a charge transfer is being produced.

In this sense, a tight confinement of the dye LDS 722 in a 1D-nanoporous host is crucial to limit its flexibility and induce an aligned arrangement of the dyes along the channels. With respect to the most representative sample (15A), the absorption spectra of the bulk powder shows the typical band of the LDS 722 dye at 397 nm ascribed to the S_0-S_1 "locally excited" (LE) transition, hypsochromically shifted respect to that recorded for the dye in solution, together with a less intense and red-shifted band (**Figure 3.6**), attributed to the ICT state in the ground state. The fact that this ICT band is detected only in the hybrid system and not in solution should be a consequence of the stabilization of the ICT state due to the rigid environment imposed by the host matrix.

Regarding fluorescence emission, hybrid samples show red fluorescence ascribed to the ICT emission band (**Figure 3.6**) but much more intense than that for the dye in aqueous solution ($\phi_{fl} = 0.17$ in powder with respect to $\phi_{fl} \approx 0.01$ in solution). Thus, a dramatic enhancement of the fluorescence capacity of the hemicyanine has been achieved through the encapsulation of the dye into AEL matrix. Indeed, fluorescence quantum yields recorded for the powder sample is more than fifteen times higher than those in aqueous solution (see
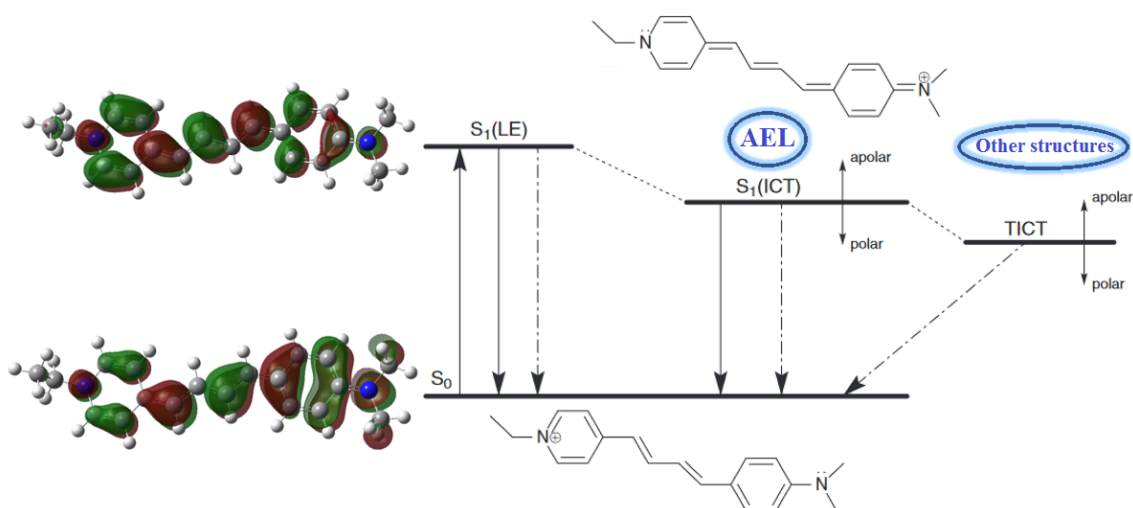
Figure 3.7: Molecular structure and electronic densities of the HOMO and LUMO states of the hemicyanine LDS 722 dye. Scheme of the intramolecular charge transfer mechanism involved upon photoexcitation. Radiative and non-radiative transitions are represented by solid and dashed lines, respectively.

data in **Table 3.4**) especially when the ICT state is directly populated (exc = 530 nm), in comparison with excitation at the LE band (exc = 410 nm). Actually, exciting the sample upon UV-blue light (i.e. exc = 410 nm), a reminiscent emission band at around 450 nm is recorded , ascribed to the radiative deactivation of LE, together with the more intense ICT emission band (**Figure 3.6**). These facts indicate that the population of the ICT in the excited state through relaxation from an excited LE state is not entirely efficient. It should be pointed out that, although those dyes whose emission takes place from ICT states usually show large Stokes shifts minimizing inner filters, the broad ICT absorption band now recorded for LDS 722/AEL material overlaps with the emission band (**Figure 3.6**), enhancing the possibility of inner-filter effect and decreasing the fluorescence capacity. Therefore, this is likely the reason why the fluorescence efficiency in samples with high dye uptake (samples 17B and 15B), has been drastically reduced.

The fluorescence decay curve registered for the sample 15A shows a biexponential behaviour with lifetimes of 2.2 ns and 0.63 ns, both of them longer to that obtained in solution (**Figure 3.6** and **Table 3.4**). The increase in the lifetime is a direct consequence of the decrease of non-radiative pathways of the LDS 722 due to the rigid medium. Note here that the longer lifetime could be ascribed to LDS 722 into AEL because of the high constraint reached in that host, and therefore the shortest decay of around 0.68 ns could

Table 3.4: Main photophysical parameters of of LDS 722/AEL (sample 15A) together with those for the dye in solution: maximum absorbance wavelength (λ_{abs}), maximum emission wavelength (λ_{fl}), Stokes shift (ΔV_{stokes}), fluorescence quantum yield (ϕ_{fl}) and fluorescence lifetimes (τ).

Sample	λ_{abs}	λ_{fl}	ΔV_{stokes} (cm^{-1})	ϕ_{fl}	τ/ns (%A)
Solution	446	715	8551	0.012 [15]	0.08
15A	401	693	10508	0.11[a]	0.63 (38)
				0.17[b]	2.21 (62)

[a]Registered under 410 nm excitation; [b]Registered under 530 nm excitation.

be ascribed to the dye embedded in other structures considered as impurities (such as AFI which has bigger pores).

Finally, **Figure 3.8** shows the polarization experiments performed in sample 15A. Those experiments provide information about the alignment of the dye inside the host. The fluorescence image shows LDS 722/AEL crystals of few micrometers with rectangular shape and a red emission colour under blue Illumination (with D470/40 band pass filter). Importantly it responds to the linear polarized light, obtaining maximum intensity for the analyzer in the direction of the channels and minimum fluorescence when it is set perpendicular to them as it can be shown in **Figure 3.8**. Taking into account that the dipolar transition moment of the LDS 722 dye is placed along the major axis of the molecule (checked by theoretical calculations), this anisotropy response indicates that Styril 722 is mostly incorporated inside the voids.
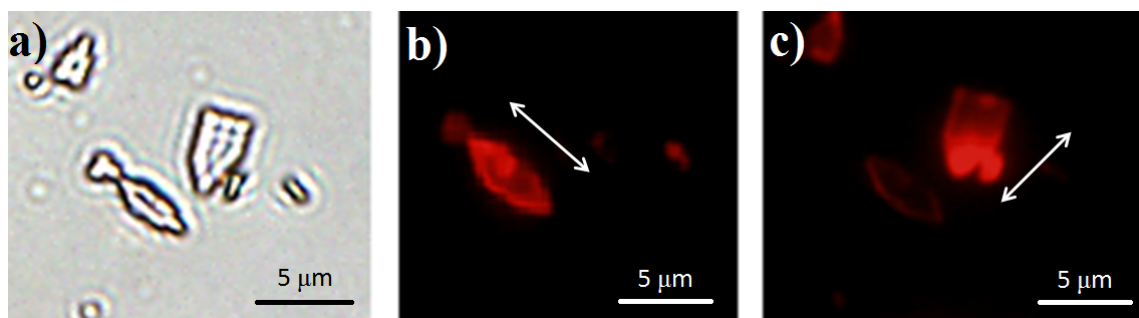

Figure 3.8: Transmission and polarized fluorescence images of sample 15A under blue excitation light for orthogonal polarizations (arrows indicate the direction of the polarized light).

In other words, a significant improvement in the photophysical properties of the dye together with an alignment along the channels of MgAPO-11 structure has been carried out successfully. However, AEL pure phase was not reached during this work. For that reason, future experiments will be carried out to optimize the synthesis in order to obtain only MgAPO-11. For this goal, several ideas have been put forward such as changing the template and playing more with the synthesis composition and reaction time (testing times between 1 hour and 2 hours or longer).

3.3 Dye occlusion into MgAPO-5 host systems

In this section, a second hemicyanine-like dye, LDS 730, homologous to LDS 722 but with a larger molecular size, is incorporated into a microporous magnesium aluminophosphate MgAPO-5, which has a higher pore size with respect to MgAPO-11. Similarly, the hybrid materials were prepared by crystallization inclusion method through hydrothermal synthesis under MW heating as in the former case, from gels with the following molar composition: 0.2 MgO: 1 P_2O_5: 0.9 Al_2O_3: 0.75 TEA: z LDS730: 305 H_2O (previously used in other works, [16]), varying the dye amount from z = 0.008 to z= 0.024 (see **Table 3.5**).

Table 3.5: Gel composition: 0.2 MgO: 1 P_2O_5: 0.9 Al_2O_3: 0.75 TEA: z LDS730: 305 H_2O and the structural phases achieved for each sample together with the initial and final pH-s. The amount of dye-loaded in each sample is expressed as mmol of dye per 100 grams of solid product and as a percentage of the dye-loaded with respect to the initial amount of the gel.

Sample	z	Phases (%)		pH		mmol/100g	Dye uptake (%)
		AFI	Impurities	Initial	Final		
A	0	51	39 Others	3.4	4.6	–	–
B	0.008	24	76 Others	3.3	4.4	0.86	19
C	0.016	46	54 Others	3.7	4.5	0.60	7
D	0.024	32	68 Others	3.3	4.4	0.95	6

It should be pointed out that according to the thermogravimetric analysis, LDS 730 dye shows an earlier degradation temperature, of 40°C with respect to LDS 722 ($\approx$ 260°C vs 300°C, respectively, calculated by the derivative of the thermogravimetric analysis, see **Figure 3.9**). As a consequence, LDS 730 dye cannot withstand temperatures higher than 170 °C in the hydrothermal synthesis via conventional heating. For this reason, a temperature of 160°C was selected for the synthesis of LDS 730/AFI much lower in comparison with the previous section for the LDS722/AEL that the temperature was rised up to 195°C. However, AFI structure is a more thermodynamically favoured structure compare with AEL, and generally, it is not necessary a very high temperature in the synthesis to reach relatively pure phase. In this context, a final phase of around 50% is obtained at 160°C without any dye in the synthesis (**Table 3.5**, **Figure 3.10**).

According to the results detailed in **Table 3.5** and **Figure 3.10** although AFI structure was obtained, its final percentage was affected when the LDS 730 was added to the synthesis gel. After the structural analysis, other impurities appear to come in the diffrac-
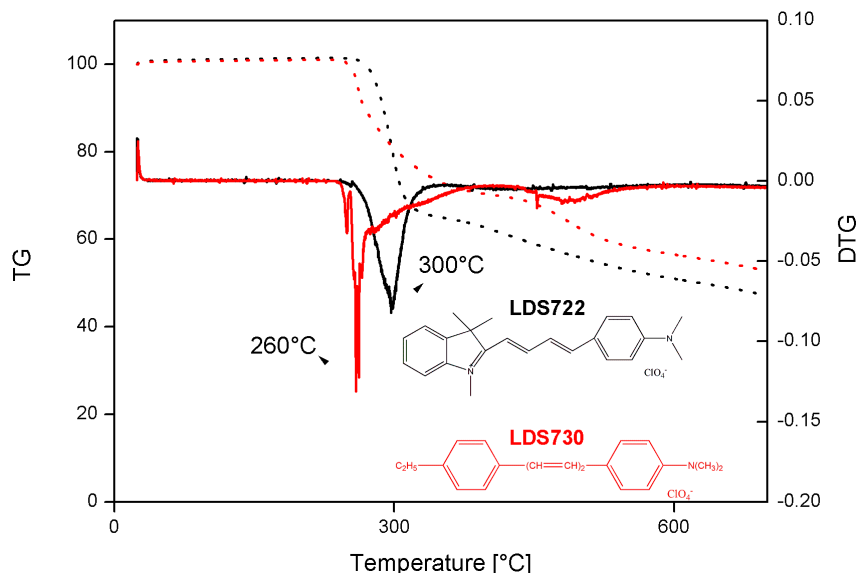
Figure 3.9: Overall thermogravimetric decomposition (TG) process of the LDS 722 and LDS 730 dyes and determination of the decomposition characteristic temperatures by the derivative thermogravimetric method (DTG).

tion patterns and are noticeable when z is 0.008 and 0.024 (Sample B and D, see the **Table 3.5** and the lower intensity in the characteristic peaks of the AFI structure at $2\theta = 7.4°$).

Moreover, the dye uptake in the host is scarce (%19 the maximum for sample B) and is even lower when a higher dye amount is added to the synthesis gel ($\approx$6-7 %). This could be a consequence of two different factors: a partial decomposition of the dye during the synthesis and/or the very tight fitting between the molecular dimensions of the dye and the pore size of the aluminophosphate may decrease the extent in the amount of the final dye occlusion. Thus, a similar dye amount was reached within the AFI pores independently of the amount of dye added to the gel **Table 3.5**. A blue light colour was obtained in the three samples which is the characteristic colour of this dye **Figure 3.10b**.

The scanning electron microscopy images (**Figure 3.11**) show two different types of crystals. Large crystals ($\approx$20 um) with hexagonal shape assigned to MgAPO-5 structure together with star-like crystals, which are ascribed to impurities. Interestingly, when the dye is added in the synthesis gel, the crystal growth of AFI structure is affected, obtaining hexagonal rings in the middle of the MgAPO-5 crystals (see **Figure 3.11b**). Furthermore, the transmission image captured by the microscope confirms these crystallising behaviours distinguishing the two crystal types: the typical blue colour for the AFI crystals while the
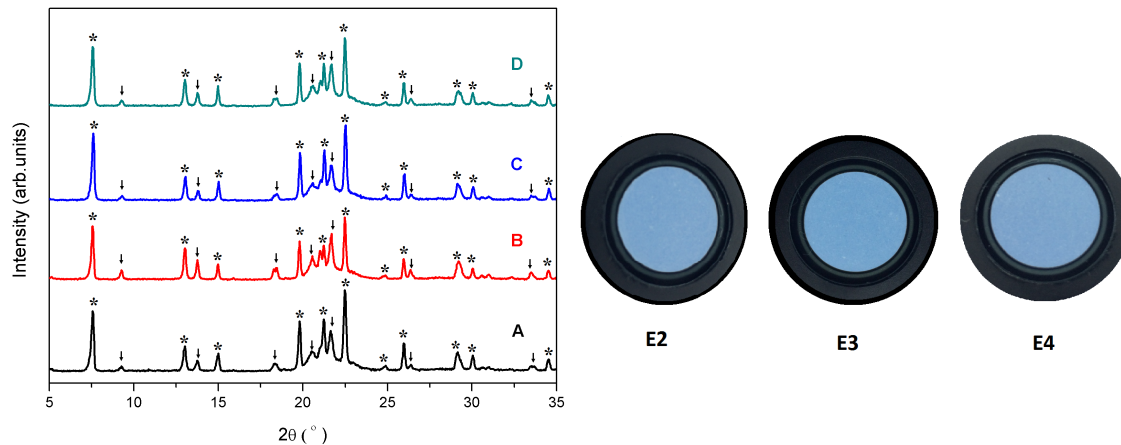
Figure 3.10: a) XRD patterns of samples A-D; marks * denote peaks from AFI phase while arrows denote peaks from impurity phases. **b)** LDS730/AFI samples under ambient light.

star-shaped crystals are colourless, indicating that in this phase the dye is not embedded (**Figure 3.11**).

On the other hand, the main photophysical parameters are shown in **Table 3.6**. In aqueous solution, LDS 730 or Styril 6 has a high absorption capacity centered at 573 nm and a reminiscent emission placed at 700 nm, showing a very large Stokes shift (3166 cm^{-1}), as a consequence of an intramolecular charge transfer (previously explained in the **Section 2.4**, as it occurs in the homologous dye LDS 722. Similarly, rotameric motions occur via different pathways around different single and double bonds which lead to several twisted intramolecular charge transfer, responsible of the poor fluorescence quantum yields and very short lifetimes of this dye in solution. Indeed, the quantum yield and the lifetime of LDS 730 in solution could not be registered because they were too low and lay under the detection limit of the spectrofluorimeter (i.e. the decay curve obtained was similar to IRF "instrument response function").

On the other hand, LDS 730/AFI bulk powders show the main absorption band at around 695 nm **Table 3.6**, very red-shifted with respect to that of the dye in aqueous solution (λ_{abs}: 573 nm, see **Figure 3.12**), which is indeed placed in the same region as the emission of the dye in solution.

This fact suggests that the intramolecular charge transfer is stabilised in the ground state giving rise to a new and red-shifted band in the absorption spectra. In fact, after
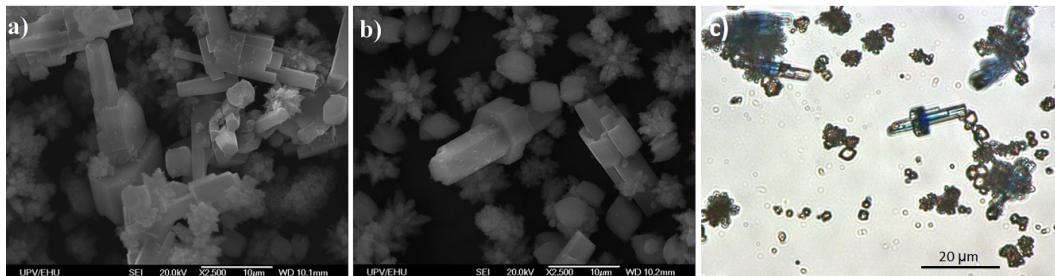
Figure 3.11: SEM micrographs of samples **a)** A, without any dye and **b)** C, with 0.016 of dye; **c)** Transmission image captured by the microscope of sample C.

the deconvolution of the absorption spectra, two Gaussian bands are derived, one centered at 614 nm ascribed to the locally excited (maroon dotted spectra) and the second band centered at 714 nm assigned to ICT (blue dotted spectra), with a relative area under the curve of 1.5:1 (LE : ICT), respectively (**Figure 3.12b**).

Table 3.6: Photophysical parameters for LDS 730/AFI samples together with those for the dye in solution: maximum absorbance wavelength (λ_{abs}), maximum emission wavelength (λ_{fl}), Stokes shift (ΔV_{Stokes}) and fluorescence average lifetimes defined in equation **2** (τ).

Sample	λ_{abs}	λ_{fl}	ΔV_{stokes} (cm^{-1})	τ/ns (%A)
Solution	573	700	3166	$\prec 0.01$
B	691	820	2277	0.35
C	695	799	1873	0.38
D	698	824	2191	0.37

In this line, the fluorescence spectrum of the bulk powder registered under 600 nm excitation show two bathochromically shifted bands with respect to the solution, at 669 nm and at 821 nm, assigned to the local excited emission (red dashed spectra) and to the ICT state (blue dashed spectra) with an area under the curve of 1:3 (LE : ICT), respectively (**Figure 3.12b**). This result is a direct consequence of the space restriction into the constricted host, which induces a planar configuration, denoted as planar ICT (PICT) state, responsible for the fluorescence emission, and minimization of the rotations and vibration motions, which are non-radiative paths that efficiently quench the fluorescence in the LDS 730 dye. Although, note here that the quantum yield could not be determined due to the lack of standard in the NIR region.

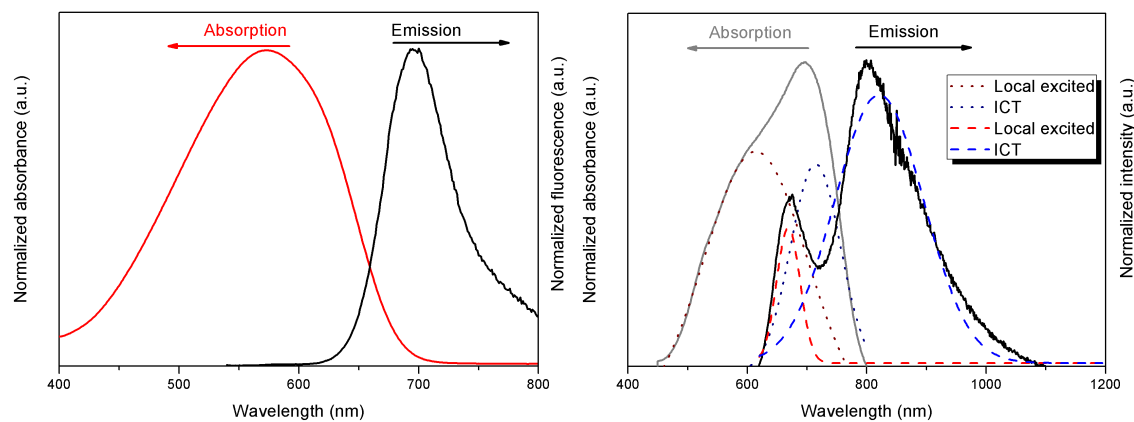It can be confirmed the decrease of non-radiative pathways by the longer lifetimes

Figure 3.12: a) Height normalised absorption (red) and emission spectra (black) recorded (excitation at 530 nm) for the dye LDS 730 in aqueous neutral solution. **b)** LDS730/AEL powder (Sample C, black) absorption and emission (excitation at 600 nm) height normalised spectra's together with the deconvolution fit of each band ascribed to the locally excited (maroon or red) and ICT(blue) states.

registered in powder with respect to the dye in solution (see **Table 3.6**, less than 0.01). It should be pointed out that due to the difficulTy to give a physical interpretation to triexponential decay curves the average lifetimes were considered (**eq. 2**).

In conclusion, a signicant improvement in the photophysical properties of the dye has been carried out successfully, enhancing 40 times the lifetime in bulk in contrast to the dye in solution.

Chapter 4

Conclusion

- By systematic variations of the conditions (time, temperature) and gel composition (Mg and SDA) of the hydrothermal synthesis via MW heating, MgAPO-11 (AEL) structure was attained as a majority phase. The optimal conditions up to now are 0.1MgO: 1 P2O5: 0.95Al2O: 1SDA: 300H2O at 195ºC for 2 hours. Further experiments will be performed in order to improve the final phase, for instance, by changing the time, temperature and the structure directing agent.

- LDS722 (2.5 x 4.5 x 17.5 Å) dye was occluded in the channels of AEL with eliptical pore size of 4 x 6.6 Å) by means of crystallisation inclusion method. The dye uptake in the host material was relatively high and the resultant hybrid material showed good optical properties such as high quantum yield together with a preferential order of LDS722 molecules along the channels, which is not possible in the solution.

- LDS730 dye (4.4 x 5.8 x 17.8 Å), with higher molecular dimensions than LDS722, was occluded into MgAPO-5 structure, with cillindrical pores of 7.3 Å, by crystallisation inclusion method, rendering a hybrid system with absorption and the emission band in the red range of the spectrum interesting for biomedical applications.

- As a final conclusion, by the tight encapsulation of hemicyanine dyes into an appropriate 1D-nanoporous host, their emission properties are enhanced. Moreover, an alignment of the dyes along the channels is induced.

Acknowledgements

Bibliography

[1] Kickelbick, G.; Hybrid materials: synthesis, characterization, and applications. *John Wiley Sons*, **2007**.

[2] Davis, M. E. ; *Accounts of chemical research*, **1993**, *26*, 111-115.

[3] Kulprathipanja, S.; Zeolites in industrial separation and catalysis. *John Wiley Sons*, **2010**.

[4] Pluth, J. J., Smith, J. V.; *Acta Crystallographica Section C: Crystal Structure Communications*, **1987**, *43*, 866-870.

[5] García, R., Martínez-Martínez, V., Sola Llano, R., López-Arbeloa, I., Perez-Pariente, J.; *The Journal of Physical Chemistry C*, **2013**, *117*, 24063-24070.

[6] Martínez-Martínez, V., García, R., Gómez-Hortiguela, L., Sola Llano, R., Perez-Pariente, J., López-Arbeloa, I.; *ACS Photonics*, **2014**, *1*, 205-211.

[7] Ch Baerlocher, Lynne B McCusker, and David H Olson. Atlas of zeolite framework types. *Elsevier*, **2007**.

[8] Sola-Llano, R., Martínez-Martínez, V., Fujita, Y., Gómez-Hortiguela, L., Alfayate, A., Ujii, H., López-Arbeloa, I.; *Chemistry-A European Journal*, **2016**, *22*, 15700-15711.

[9] Zhang, J., Wu, H., Zhao, A., Bai, X., Kikhtyanin, O. V., Wu, W., Zhang, R.; *Journal of Porous Materials*, **2017**, 24, 437-442.

[10] Grellmann, K. H.; *Angewandte Chemie*, **1985**, 97, 138-139.

[11] Phillips, D., Drake, R. C., O'Connor, D. V., Christensen, R. L.; Time correlated single-photon counting (TCSPC) using laser excitation, **1985**.

[12] Rurack, K., Hoffmann, K., Al-Soufi, W., Resch-Genger, U.; *The Journal of Physical Chemistry B*, **2002**, *106*, 9744-9752.

[13] Wiederrecht, G. P., Sandi, G., Carrado, K. A., Seifert, S.; *Chemistry of materials*, **2001**, *13*, 4233-4238.

[14] M. J. Frisch, G. W. Trucks, H. B. Schlegel, G. E. Scuseria, M. A. Robb, J. R. Cheeseman, G. Scalmani, V. Barone, B. Mennucci, G. A. Petersson et al., Gaussian 09 (Gaussian, Inc., Wallingford, CT, 2009).

[15] Cerd L., Costela, A., GarcMoreno, I., Baos, J., L-Arbeloa, I.; *Laser Physics Letters*, **2012**, *9*, 426.

[16] Martínez-Martínez, V., García, R., Gómez-Hortiguela, L., Pérez-Pariente, J., López-Arbeloa, I.; *Chemistry-A European Journal*, **2013**, *19*, 9859-9865.